

## Article

# New Insights of Infiltration Process of Argyrodite $\text{Li}_6\text{PS}_5\text{Cl}$ Solid Electrolyte into Conventional Lithium-Ion Electrodes for Solid-State Batteries

Artur Tron \*, Andrea Paoella and Alexander Beutl \*

AIT Austrian Institute of Technology GmbH, Center for Low-Emission Transport, Battery Technologies, Giefinggasse 2, 1210 Vienna, Austria

\* Correspondence: artur.tron@ait.ac.at (A.T.); alexander.beutl@ait.ac.at (A.B.);  
Tel.: +43-664-88904356 (A.T.); +43-664-88390656 (A.B.)

**Abstract:** All-solid-state lithium-ion batteries based on solid electrolytes are attractive for electric applications due to their potential high energy density and safety. The sulfide solid electrolyte (e.g., argyrodite) shows a high ionic conductivity ( $10^{-3} \text{ S cm}^{-1}$ ). There is an open question related to the sulfide electrode's fabrication by simply infiltrating methods applied for conventional lithium-ion battery electrodes via homogeneous solid electrolyte solutions, the structure of electrolytes after drying, chemical stability of binders and electrolyte, the surface morphology of electrolyte, and the deepening of the infiltrated electrolyte into the active materials to provide better contact between the active material and electrolyte and favorable lithium ionic conduction. However, due to the high reactivity of sulfide-based solid electrolytes, unwanted side reactions between sulfide electrolytes and polar solvents may occur. In this work, we explore the chemical and electrochemical properties of the argyrodite-based film produced by infiltration mode by combining electrochemical and structural characterizations.

**Keywords:**  $\text{Li}_6\text{PS}_5\text{Cl}$ ; solid electrolyte; ethanol; cathode; NCM; infiltration route; all-solid-state battery



**Citation:** Tron, A.; Paoella, A.; Beutl, A. New Insights of Infiltration Process of Argyrodite  $\text{Li}_6\text{PS}_5\text{Cl}$  Solid Electrolyte into Conventional Lithium-Ion Electrodes for Solid-State Batteries. *Batteries* **2023**, *9*, 503. <https://doi.org/10.3390/batteries9100503>

Academic Editor: Hirotoshi Yamada

Received: 10 September 2023

Revised: 21 September 2023

Accepted: 25 September 2023

Published: 4 October 2023



**Copyright:** © 2023 by the authors. Licensee MDPI, Basel, Switzerland. This article is an open access article distributed under the terms and conditions of the Creative Commons Attribution (CC BY) license (<https://creativecommons.org/licenses/by/4.0/>).

## 1. Introduction

All-solid-state batteries (ASSBs) have attracted much attention due to their increased safety, chemical and electrochemical stabilities, and high energy density [1–3]. While progressing for the next generation, ASSBs need to find suitable parameters in the development and improvement of the solid electrolytes (SEs) that are key materials for reaching the desired performance [4,5]. Several kinds of solid electrolytes have been proposed in the literature such as Oxide- of  $\text{Li}_2\text{O}-\text{M}_x\text{O}_y$  [6,7], LIPON- [8], LISICON- [9,10], NASICON- [11], Garnet- [12], Perovskite- [13], Halide- [14], and Argyrodite-type electrolytes [15]. The latter are especially promising due to their high ionic conductivities ( $10^{-3} \text{ S cm}^{-1}$ ) and good cycling performances [16]. Although sulfide-based electrolytes are unstable in the air atmosphere [17,18], significant progress was reported in the literature related to the development of the cathodes and electrolyte films based on  $\text{Li}_6\text{PS}_5\text{Cl}$  (LPSC) sulfide electrolytes via dry- or wet-chemistry processing [19–22]. One of the remaining challenges is to mitigate the poor affinity between cathode and electrolyte particles, which leads to large interfacial resistances, high polarization, and low specific capacities due to the unwanted side reactions including the decomposition of the sulfide electrolytes observed at high voltage ranges [23]. However, comparing oxide- and sulfide-type electrolytes shows that while the oxide electrolyte has excellent chemical and electrochemical stabilities, its processability is poorer. Sulfide-based electrolytes, on the other hand, have made significant progress in dry- and wet-chemistry production of the cathode and electrolyte films [24–26].

Dry processing for the fabrication of electrolyte and cathode films presents some critical issues regarding scalability. The resulting poor mechanical properties limit their

practical usability [23,27]. Therefore, wet-chemical processing for the preparation of small- and large-scale cathodes, anodes, and electrolyte films is deemed to be more scalable than dry processing. However, the main issue related to films prepared via wet chemistry routes is the high chemical reactivity of sulfide electrolytes towards conventionally used solvents and binders, as previously reported [19,23,28–30].

As mentioned above, the control of all possible side reactions becomes pivotal to the production of films; however, few solvents and binders show low reactivity toward sulfide electrolytes [28,31,32]. In order to overcome these issues, infiltration of the solid electrolyte in porous electrodes prepared by a standard slurry coating (as established in conventional lithium-ion battery technologies) may represent a valuable alternative. Promising reports regarding this approach are available in the literature [33–35]. It should be noted that the infiltration method exploits the solubility of sulfide electrolytes in ethanol (EtOH) and is assumed to ensure high electrochemical performance as it reduces the number of toxic sulfide electrolytes, resolves cost issues, and consequently leads to an increase in energy density. In order to realize these promises, the processing parameters need to be optimized in order to obtain a homogeneous sulfide electrolyte solution capable of filling all the pores while using a minimal amount of it.

In this work, we re-evaluate the infiltration method for the preparation of composite cathodes using the Li<sub>6</sub>PS<sub>5</sub>Cl sulfide electrolyte as a model system. An electrolyte solution using ethanol as the main solvent was prepared and infiltrated into the tortuous pores of LiNbO<sub>3</sub>-coated LiNi<sub>0.8</sub>Co<sub>0.1</sub>Mn<sub>0.1</sub>O<sub>2</sub> (NCM811-LiNbO<sub>3</sub>) electrodes. Moreover, some parameters for the electrolyte infiltration such as the effect of co-solvents, Li<sub>6</sub>PS<sub>5</sub>Cl content in the solution, and applied temperatures were studied and their impact on the electrode properties (porosity, distribution of sulfide electrolyte) was determined. A high filling degree of the cathode and increased ionic and electrical contact were the targets of process optimization. However, it could be shown that a simple infiltrating method applied to conventional electrodes, as used in lithium-ion batteries (LIBs), remains a challenge. Several parameters need to be controlled, like the structure of electrolytes after drying, the chemical stability of binders and electrolytes, and the nature of infiltrated electrolytes to encourage good lithium ionic conduction.

## 2. Materials and Methods

**Electrode preparation –** The NCM cathodes were prepared by first blending the obtained poly-crystalline powders (LiNi<sub>0.8</sub>Co<sub>0.1</sub>Mn<sub>0.1</sub>O<sub>2</sub> coated by LiNbO<sub>3</sub> 1 wt%, NEI corp.) (92 wt%), polyvinylidene fluoride (Sigma-Aldrich) binder (4 wt%), and carbon black (Super C65, Imerys) electronic conductor (4 wt%) in N-methyl pyrrolidone (NMP, Sigma-Aldrich) via centrifugal planetary mixing (THINKY MIXER, ARE-250) to obtain a uniform slurry. This was further cast onto aluminum foil (thickness = 15 µm) and dried at 120 °C for 10 min to remove the NMP solvent; the electrode sheets were calendered to ensure good interparticle contact and to reduce their porosity. By setting the calender gap to smaller sizes, electrodes with less porosity could be prepared. Thus, electrodes exhibiting porosities of 70%, 60%, 50%, and 40% were obtained. The porosities of the electrodes were estimated by subtracting the total volume of all pristine components from the volume of the prepared electrodes. The latter was determined by measuring the thickness of circular cut-outs (15 mm diameter) with a µm gauge. Finally, all electrodes were dried at 120 °C for 16 h in a vacuum oven before being transferred into an Ar-filled glovebox (H<sub>2</sub>O = 0.3 ppm; O<sub>2</sub> ≤ 0.1 ppm). The infiltration process and all further handling were also conducted in an Ar-filled glovebox unless otherwise stated.

**Infiltration process –** For the preparation of solid electrolyte solutions, Li<sub>6</sub>PS<sub>5</sub>Cl (NEI corp.) was dissolved into ethanol (Sigma-Aldrich), and mixtures of ethanol with anisole (Sigma-Aldrich) and ethyl acetate (Sigma-Aldrich) at 0.5, 5, and 11 wt% of electrolyte (further referred to as SE solution).

For the fabrication of composite cathodes, the as-prepared coated NCM811-LiNbO<sub>3</sub> electrodes were infiltrated with the SE solutions by immersion/dip coating processes. The infiltration route exploits the solubility of the Li<sub>6</sub>PS<sub>5</sub>Cl material in ethanol and recrystallization of the same after evaporation of the solvent. Drying of the electrodes was first conducted at room temperature by applying a vacuum, followed by an increase in temperature to 120 °C, which was kept for 2 h. Thus, a composite electrode (solid electrolyte + electrode) is obtained, which can further be used in the same way as composite electrodes processed by conventional methods. A schematic of the infiltration route is shown in Figure 1.

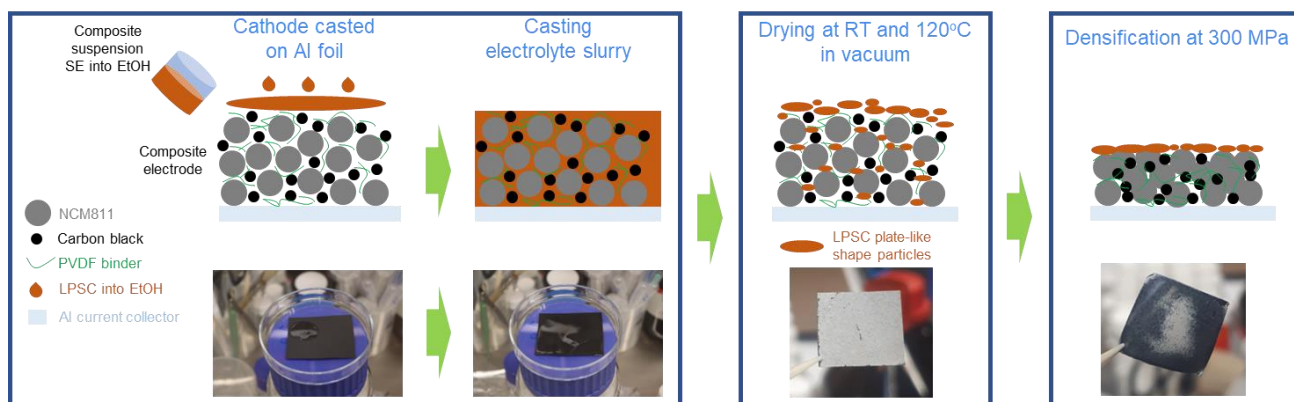


**Figure 1.** Schematic illustration of the infiltration process of sulfide-based solid-electrolyte (Li<sub>6</sub>PS<sub>5</sub>Cl) in ethanol solvent into conventional NCM811-based cathode.

**Wettability**—The wettability of as-prepared and infiltrated cathode samples was qualitatively determined by visual evaluation of optical photographs taken 30 s after dropping the Li<sub>6</sub>PS<sub>5</sub>Cl-ethanol solution on top of the cathodes.

**Ionic conductivity**—The ionic conductivities of the pristine solid electrolyte powders, powders obtained after treatment with ethanol, and powders obtained after solvent treatment and subsequent drying at 80 °C and 180 °C for 2 h were measured by AC impedance spectroscopy. The powder samples were placed between two stainless-steel rods within a polyetherether ketone (PEEK) liner/template with a 16 mm diameter and pressed at 6 tons for 5 min (approximately 300 MPa). Then the pressure was released to 0 MPa and the impedance was measured with increasing pressure. The thickness of the pellet was around 1.0 mm depending on the amount of powder used. All sample preparation steps were performed inside an Ar-filled glovebox. Electrochemical impedance spectroscopy (EIS) was performed at room temperature using an AMETEK VersaSTAT MC from 1 MHz to 1 Hz with an amplitude of 10 mV in potentiostatic (PEIS) mode.

**Powder X-ray diffraction, Scanning electron microscopy, and Wavelength-dispersive X-ray fluorescence**—The crystal structure of the solid electrolyte powders and NCM cathodes (pristine and infiltrated) was determined by X-ray diffraction (XRD) analysis using a PANalytical X'Pert Pro diffractometer in Bragg-Brentano geometry with Cu K $\alpha$  radiation (45 kV, 40 mA) in a 2 $\theta$  range of 5–80° at a scan rate of 0.03° s<sup>-1</sup>. The samples for the XRD measurements were prepared and sealed in a glove box filled with Ar using a sample holder with a polymer cap. The polymer cap shows a broad peak around 20°2 $\theta$ , which can be seen in all diffraction patterns.

The surface morphology of the samples before and after treatment was observed by field emission scanning electron microscopy (FE-SEM, ZEISS Supra 40) with energy-dispersive X-ray spectroscopy (EDX).

Furthermore, the elemental composition of the NCM powder was determined using wavelength-dispersive X-ray fluorescence (WDXRF, Zetium, Panalytical, The Netherlands). The samples were irradiated with X-ray emission provided by a Rh tube with a maximum power of 4000 W, maximum voltage of 60 kV, and maximum current of 125 mA. The research was performed with the application of a fine collimator, analyzing crystal LiF200 (0.124 Å), and a scintillation counter as a detector (SC). For all elements evaluated in this study, only the electronic transition, K $\alpha$ , was considered.

Electrochemical testing of the infiltrated cathode—For electrochemical tests, a lithium metal anode (MTI, Li chips, diameter of 15.6 mm, thickness of 0.25 mm) was used as a counter electrode. The method used to prepare the lithium metal anode is described in [26]. To prepare the bilayers, 320 mg of electrolyte powder is placed in a Ø16 mm pellet die and pressed at 50 MPa for a few seconds. Then the infiltrated cathode (loading of 1 mAh cm $^{-2}$  and approximately 8–9 mg cm $^{-2}$ ) is placed on the solid electrolyte surface from one side and compacted at a pressure of 300 MPa. The pressure is maintained for 5 min. The lithium metal anode was then put on the opposite side of the solid electrolyte pellet. The final cell was placed in the cell holder and a pressure of 10 MPa was applied during the measurements. A Gamry Interface 1010E was used for the galvanostatic cycling measurements. A current density of 0.05 mA cm $^{-2}$  (C/20) in the potential range of 4.3 V and 2.7 V (vs. Li/Li $^{+}$ ) was applied. Electrochemical impedance spectroscopy (EIS) was performed from 2 MHz to 10 Hz at 10 mV amplitude in PEIS mode.

### 3. Results

First, the commercial poly-crystalline cathode material, i.e., NCM811 coated by LiNbO<sub>3</sub>, which has been previously used for all-solid-state batteries [27,36,37], was characterized via physicochemical and electrochemical methods as shown in Figure S1a (Supplementary Information). It should be noted that the obtained XRD pattern corresponds to the R-3m hexagonal structure of  $\alpha$ -NaFeO<sub>2</sub> (which corresponds to the LiNiO<sub>2</sub> (JCPDS 74–0919) structure used for indexing the peaks), and all of the peaks are well-assigned using this structure type [38–40]. However, the coating material LiNbO<sub>3</sub> on the surface of NCM811 is not observed in the XRD patterns. It is assumed that due to the low crystallinity and low rel. amount of LiNbO<sub>3</sub> coatings, no diffraction pattern can be obtained using conventional X-ray sources [36,40]. Figure S1b (Supplementary Information) shows the surface morphology of the NCM811-LiNbO<sub>3</sub> sample. A clean and smooth surface can be seen. Spherical secondary particles with a size of approximately 10–15  $\mu$ m and primary particles with a size of approximately 200–500 nm were observed. To confirm the presence of Ni, Mn, Co, and Nb elements, XRF measurements were conducted. The analysis showed that Ni, Mn, and Co show the expected molar ratio of close to 8:1:1, and the amount of Nb was determined as 0.97 wt.%. Electrochemical analysis of the NCM811-LiNbO<sub>3</sub> cathode was additionally tested in a liquid electrolyte (1 M LiPF<sub>6</sub> in EC:DEC, 1:1 v/v) as shown in Figure S1c,d (Supplementary Information). The rate performance of the NCM811-LiNbO<sub>3</sub> cathode was evaluated by applying various current densities of 0.1, 0.2, 0.5, 1, 2, and 5C (at a loading of 1 mAh cm $^{-2}$ ) each for five cycles in a potential range of 3.0–4.3 V. High specific charge values of 160 mAh g<sub>NCM</sub> $^{-1}$  at 0.1C and close to 100 mAh g<sub>NCM</sub> $^{-1}$  at 5C could be obtained.

In wet chemistry film production, the solvent has an impact on the microstructure and distribution of components of the cathode. For example, binder migration might have a considerable impact on cell performance [41]. Thus, the chemical properties of solvents (Table S1, Supplementary Information) like vapor pressure, density, boiling point, and possible safety hazards need to be taken into account.

To prepare the SE solution, the  $\text{Li}_6\text{PS}_5\text{Cl}$  electrolyte was dissolved in ethanol upon which a brown solution was obtained [34], as shown in Figure S2 (Supplementary Information). Different concentrations of the SE solutions were prepared. The color of the obtained solutions did not change compared to the one with the highest amount of the electrolyte, i.e., 11 wt.% (cf. Figure 2). However, the surface morphologies of the received powders after treatment with the solvent and subsequent drying changed with the used  $\text{Li}_6\text{PS}_5\text{Cl}$  concentration. It should be noted that the  $\text{Li}_6\text{PS}_5\text{Cl}$  solutions can exhibit different colors depending on the chain lengths of the formed polysulfides, the concentration, and the kind of solvent used [19]. The ethanol solvent was left to evaporate from the SE solutions at room temperature and the sample was further dried at 80 °C and 180 °C for 2 h. The XRD patterns of the as-prepared powders match well with the one for the argyrodite phase. This phase can be retrieved as the main component at 80 °C; however, some impurity phases are visible as additional peaks in the diffraction patterns (Figure 2) emerge. After heating at 180 °C, the intensity of the peaks corresponding to the electrolyte increases due to an increase in crystallinity/crystallite size. Some of the impurity phases ( $\text{Li}_2\text{S}$ ,  $\text{LiCl}$ , and/or  $\text{Li}_3\text{PO}_4$ ) are consumed, although not all of them. The additional phases indicate side reactions, which could form resistive interlayers at the cathode and solid electrolyte interface [42]. During the drying steps, changes in the stoichiometry of the SE solution occur due to the formation of stable, unwanted components such as lithium sulfide and lithium chloride, as well as the potential loss of sulfur due to the formation of  $\text{H}_2\text{S}$ . It is reported that, in general, even higher temperatures (>500 °C) are required to fully recover the argyrodite phase from these side products [43]. However, regarding the thermal stability limit of the cathode (especially of the polymer binder), heat treatment above 500 °C is not feasible as decomposition of the components occurs and side reactions like cation exchange reactions can be catalyzed (Metal oxide from/to Metal sulfide exchange).

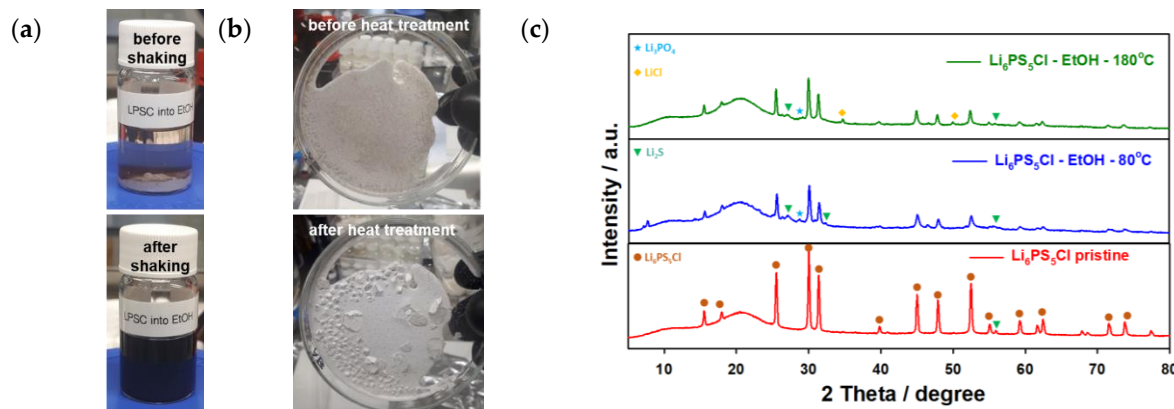


**Figure 2.** Solution of solid electrolyte of  $\text{Li}_6\text{PS}_5\text{Cl}$  into ethanol (a) before and after shaking; (b) Solid electrolyte treated with ethanol and depicted after drying at RT and after 180 °C for 2 h, (c) XRD patterns of the pristine  $\text{Li}_6\text{PS}_5\text{Cl}$  materials and after treatment with ethanol and subsequent drying at 80 °C and 180 °C.

The treated electrolyte powders were also evaluated by EIS measurements to determine the impact of the solvent treatment and subsequent drying procedure on the ionic conductivity of the samples. The powders were pelletized and sandwiched between lithium-ion blocking stainless steel (SS) electrodes in an SS | solid electrolyte | SS setup, as shown in Figure 3. The Nyquist plots of the samples are presented in Figure S3 (Supplementary Information). The samples after ethanol treatment show an additional semi-circle in the corresponding Nyquist plots. This additional impedance source is associated with the grain boundary resistances related to the particle–particle contact area. It seems that interparticle contact has been reduced after the solvent treatment and thus higher impedance values and lower ionic conductivities compared to the pristine sample are observed. All ionic conductivities are increased with increasing pressure applied to the measuring cell,

similar to the pristine electrolyte. After ethanol treatment and drying at 80 °C, the ionic conductivity drops by around two orders of magnitude. It is estimated that the impurities observed in the XRD patterns are mainly located on the surface of the electrolyte particles, leading to high interfacial resistances (grain boundary) as reported in [44]. By contrast, after drying at 180 °C, the ionic conductivity only decreases to  $10^{-4}$  S cm<sup>-1</sup>, i.e., a drop of around one order of magnitude compared to the pristine powder. The ionic conductivities determined in this work are similar to values reported for ethanol-treated Li<sub>6</sub>PS<sub>5</sub>Cl [45]. Previous reports also showed that ethanol treatment has an impact on the ionic conductivity of the solid electrolyte due to the formation of impurity phases [46–49]. The lower ionic conductivity ( $10^{-5}$  S cm<sup>-1</sup>) is attributed to an increase in grain boundary resistance. The ionic conductivity values reported here are comparable with the ones reported in [33–35], which used the infiltration method for the preparation of composite Li<sub>6</sub>PS<sub>5</sub>Cl anodes and cathodes, as shown in Table 1. Moreover, the density of the obtained powder pellets (densified at 300 MPa), which were used for the ionic conductivity measurements, was compared, and a significantly lower density was obtained for the ethanol-treated samples compared to the pristine powder (theoretical value for Li<sub>6</sub>PS<sub>5</sub>Cl 1.64 g cm<sup>-3</sup> [50]) (Figure 3b and Table 1). The mechanical properties of the obtained material after solvent treatment might be quite different from the commercial Li<sub>6</sub>PS<sub>5</sub>Cl, especially in terms of hardness and plasticity. This is expected due to the influence of the impurity phases. Thus, densification by cold-pressing might yield significant differences in the quality of the prepared powder pellets and, consequently, samples with impurities seem to exhibit a higher degree of defects and porosity. This could further explain the lower ionic conductivities observed for the ethanol-treated samples.

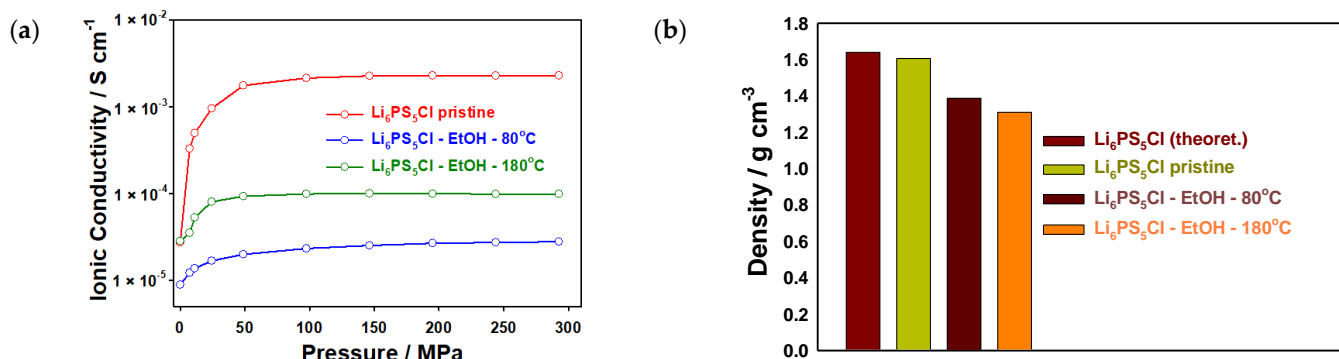


**Figure 3.** (a) Ionic conductivities and (b) density of powder pellets (densified at 300 MPa) used for EIS measurements of Li<sub>6</sub>PS<sub>5</sub>Cl samples as well as after treatment with ethanol and subsequent drying at 80 °C and 180 °C for 2 h, and without treatment.

The SEM images of the as-prepared Li<sub>6</sub>PS<sub>5</sub>Cl samples after ethanol treatment and without treatment were recorded to document any changes in the morphology of the samples as shown in Figure 4. The SEM images indicate that the morphology of Li<sub>6</sub>PS<sub>5</sub>Cl samples changes considerably upon ethanol treatment (shown in Figure 4a–d). For low concentrations of the electrolyte in the SE solutions, the morphology of the obtained particles is comparable to the pristine compound; however, more agglomerates can be observed. Furthermore, small platelets are visible, which indicate impurity phases like Li<sub>2</sub>S that usually crystallize in an anisotropic shape [51]. At higher concentrations of the SE solutions, the impurity phases even increase. Furthermore, a shift from the elemental stoichiometry of the pristine phase is observed for samples obtained after the solvent treatment, cf. Figure 4. These observations confirm the previous assumptions that the impurity phases interfere with the precipitation process of the stoichiometric Li<sub>6</sub>PS<sub>5</sub>Cl phase and that they can also impact the processability of the sample due to the difference in mechanical properties. It should be noted that after ethanol solvent treatment, the stoichiometry of elements is changed due to the possible formation of the side reaction

components ( $\text{Li}_2\text{S}$ ,  $\text{LiCl}$ , and/or  $\text{Li}_3\text{PO}_4$ ) and structure changes (Figure 2). Additionally, the presence of possible carbon on the surface of LPSC particles can be related to the formation of a carbon layer as an electronic conductive source, which can have a crucial effect on the performance (in particular on ionic conductivity, Table 1) of the LPSC electrolyte after solvent treatment. It should be noted that due to the inert synthesis conditions, which result in residual carbon from the precursors, the presence of C on the surface of the obtained samples is common to all electrode materials. Furthermore, EDS analysis revealed the presence of a possible carbon coating on the surface solid electrolyte. Thermogravimetric analysis (TGA) confirmed the presence of carbon on the surface of the materials [52]. Due to the possible formation of undesirable compounds above 600 °C in the air, the mass of the samples decreased to a small amount during TGA [53]. Thus, the amount of carbon on the surface of the samples had no significant effect on the electrochemical performance when the amount of carbon was below 5% by weight for materials subjected to the coating process in an inert atmosphere. However, for the heat treatment of the LPSC electrolyte over EtOH as a polar solvent with different concentrations, this effect was observed for the obtained samples (Figure 4 and Table 1).

**Table 1.** Reported data of ionic conductivity of sulfide solid electrolytes prepared by \* dissolution–reprecipitation process via ethanol solution.

Sulfide Electrolyte	Solvent	Post-Treatment (Heating Up to XX °C under Vacuum)	Ionic Conductivity after Dissolution, $\text{S cm}^{-1}$ *	Density of Powder Pellets (Densified at 300 MPa), $\text{g cm}^{-3}$	Reference
$\text{Li}_6\text{PS}_5\text{Cl}$ , 0.4Li-0.6Li <sub>4</sub> SnS <sub>4</sub>	Ethanol, Methanol	180	$1.9 \times 10^{-4}$	-	[33]
$\text{Li}_6\text{PS}_5\text{Cl}$	Ethanol	180	$10^{-4}$	-	[34]
$\text{Li}_6\text{PS}_5\text{Cl}$	Ethanol	180	$10^{-4}$	-	[35]
$\text{Li}_6\text{PS}_5\text{Cl}$	Ethanol	150	$4 \times 10^{-5}$	-	[46]
$\text{Li}_6\text{PS}_5\text{Cl}$	Ethanol	150	$6 \times 10^{-5}$	-	[47]
$\text{Li}_6\text{PS}_5\text{Cl}$	Ethanol	150	$3 \times 10^{-4}$	-	[48]
$\text{Li}_6\text{PS}_5\text{Cl}$	Ethanol	80	$1.4 \times 10^{-5}$	-	[49]
$\text{Li}_6\text{PS}_5\text{Cl}$ pristine			$2.14 \times 10^{-3}$	1.61	This work
$\text{Li}_6\text{PS}_5\text{Cl}$	Ethanol	80	$2.32 \times 10^{-5}$	1.39	This work
$\text{Li}_6\text{PS}_5\text{Cl}$	Ethanol	180	$9.87 \times 10^{-5}$	1.31	This work

Different ad-solvents to ethanol, i.e., ethyl acetate and anisole, were also tested to evaluate their influence on the morphology of the obtained electrolyte powders. The results are shown in Figure S4 (Supplementary Information). Samples using ethyl acetate as an ad-solvent showed larger particles and more agglomerates, whereas samples prepared by anisole as an ad-solvent showed similar morphology to samples prepared without ad-solvents. However, no difference in the obtained ionic conductivities was observed. Even after different solvent treatments, the solid electrolyte morphologies still show agglomeration of particles and changes in the surface morphologies; moreover, the XRD patterns of the ad-solvent-treated samples show changes in the diffraction patterns, and additional peaks can be observed. These indicate impurity phases such as  $\text{Li}_2\text{S}$ ,  $\text{LiCl}$ , and/or  $\text{Li}_3\text{PO}_4$  as shown in Figure S5 (Supplementary Information).

Obtaining high ionic conductivity of the infiltrated electrolyte is important as lower amounts of the electrolyte are expected to be used for the preparation of composite electrodes, compared to more conventional dry and wet processing (for which at least 30 wt% of the electrolyte are used in the relative composition of the electrodes). The obtained ionic conductivities after solvent treatment, though, leave some doubt for applicability in composite electrodes, as low specific capacities and low loading levels are expected. This is at odds with earlier reports on the feasibility of the infiltration route [35]. Nevertheless, electrochemical performance depends on many parameters affected by the resulting elec-

tolyte, such as particle sizes of the electrolyte and cathode active material, the porosity of the electrode, and the morphology of electrolyte particles after the infiltration process.

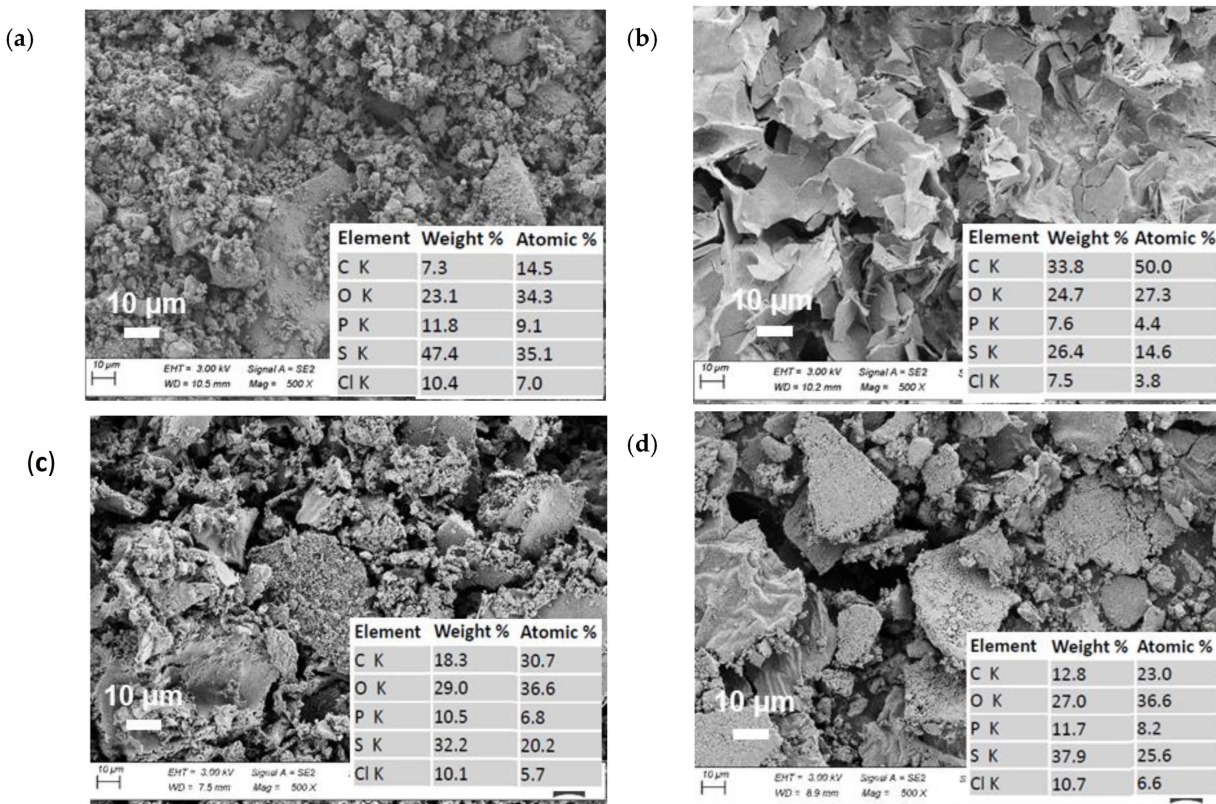


**Figure 4.** SEM images and EDX analysis of (a) pristine  $\text{Li}_6\text{PS}_5\text{Cl}$ , (b) 11 wt%, (c) 5 wt%, and (d) 0.5 wt% of solid electrolyte after ethanol treatment and drying at 180 °C.

Despite the low ionic conductivities obtained after ethanol treatment, attempts to infiltrate the  $\text{Li}_6\text{PS}_5\text{Cl}$  into conventional, porous electrodes were conducted to evaluate the wettability and pore impregnation of the SE solution. The infiltration process of the electrolyte into conventional NCM811 cathodes with different porosity levels is shown in Figure S6 (Supplementary Information). It should be noted that wettability and pore infiltration are influenced by the porosity level of the cathode, as well as by the surface tension of the used solvent (therefore, ad-solvents were tested). Depending on the capillary effect, the depth of infiltration into the porous electrodes can be tuned. Therefore, the cathodes were densified with different gap sizes to reach porosities of 70%, 60%, 50%, and 40% for estimating their wettability by dropping the  $\text{Li}_6\text{PS}_5\text{Cl}$ -ethanol solutions on top of the cathode surfaces as depicted in Figure S7 (Supplementary Information). Some characteristic properties and the wettability of the tested cathodes are summarized in Table 2.

**Table 2.** Overview of characteristics and wettability of electrodes used for infiltration route.

Porosity of Pristine Cathodes	70%	60%	50%	40%
Loading level of electrode, $\text{mg cm}^{-2}$	8–9	8–9	8–9	8–9
Loading of SE, $\text{mg cm}^{-2}$	3.34	4.27	3.59	2.08
Thickness of electrode, $\mu\text{m}$	57	51	38	28
Wettability with electrolyte solution	Very good	Good	Medium	Poor

It should be noted that the  $\text{Li}_6\text{PS}_5\text{Cl}$  electrolyte could not be completely retrieved from the solution without annealing the samples at high temperatures ( $>500$  °C) as was

reported in [42,44,54]. Even after the heat treatment, some impurities of LiCl and Li<sub>2</sub>S remain, which would have an impact on the ionic conductivity and surface morphology of the electrolyte. In order to understand the role of the porosity of conventional electrodes for the infiltration process thoroughly, we prepared four types of electrodes with different porosities and thicknesses. The electrodes were dipped into the SE solution and thermally treated under a vacuum to fully remove the residual solvent. The fabrication of the SE-infiltrated NCM811-LiNbO<sub>3</sub> electrode was completed by pressing the composite at 300 MPa to improve the contact between the active materials and electrolyte particles as shown in Figure S7 (Supplementary Information). As expected, the electrode with the highest porosity (non-densified, 70% porosity) showed the best wettability (Figure S6, Supplementary Information). When the porosity of the electrodes is reduced, though, the wettability also decreases. Electrodes with porosities <60% showed poor wettability, and the Li<sub>6</sub>PS<sub>5</sub>Cl solution quickly flowed off the cathode surfaces. Subsequently, the electrodes were coated with the Li<sub>6</sub>PS<sub>5</sub>Cl solution deposited drop-by-drop to cover the whole surface. Subsequent drying at RT and 120 °C for 2 h in a vacuum yielded the final coated/impregnated electrodes. However, due to the thermal stability of the PVDF binder used for conventional electrodes, the heat treatment of the solid electrolyte-infiltrated electrodes could not be performed at temperatures over 180 °C. The ionic resistance of the coatings was determined by EIS measurements of densified (uniaxially pressed at 300 MPa) samples using Li metal as a counter electrode and will be discussed below. XRD measurements were further conducted to depict any changes in the crystal structure of either the NMC811 material or the Li<sub>6</sub>PS<sub>5</sub>Cl. These are shown in Figure 5 and show slight changes. For Li<sub>6</sub>PS<sub>5</sub>Cl, only peaks with low intensities could be assigned. The XRD results indicate a slight chemical interaction between the NCM cathode and the SE solutions, which changes the XRD patterns. The changes remain even after heat treatment at 120 °C. After the solidification of Li<sub>6</sub>PS<sub>5</sub>Cl, only minor changes could be detected during the drying step at elevated temperatures, as was confirmed by XRD analysis (Figure 5). To verify that the Li<sub>6</sub>PS<sub>5</sub>Cl indeed penetrated the pores of NCM electrodes, cross-sections of the electrodes were prepared using a scalpel and further investigated using SEM-EDX measurements. The cross-sections and surface morphologies of infiltrated electrodes before and after densification are shown in Figure 6. However, the electrolyte seemed to be only superficially applied to the electrodes, and no relevant penetration into the electrode could be observed.

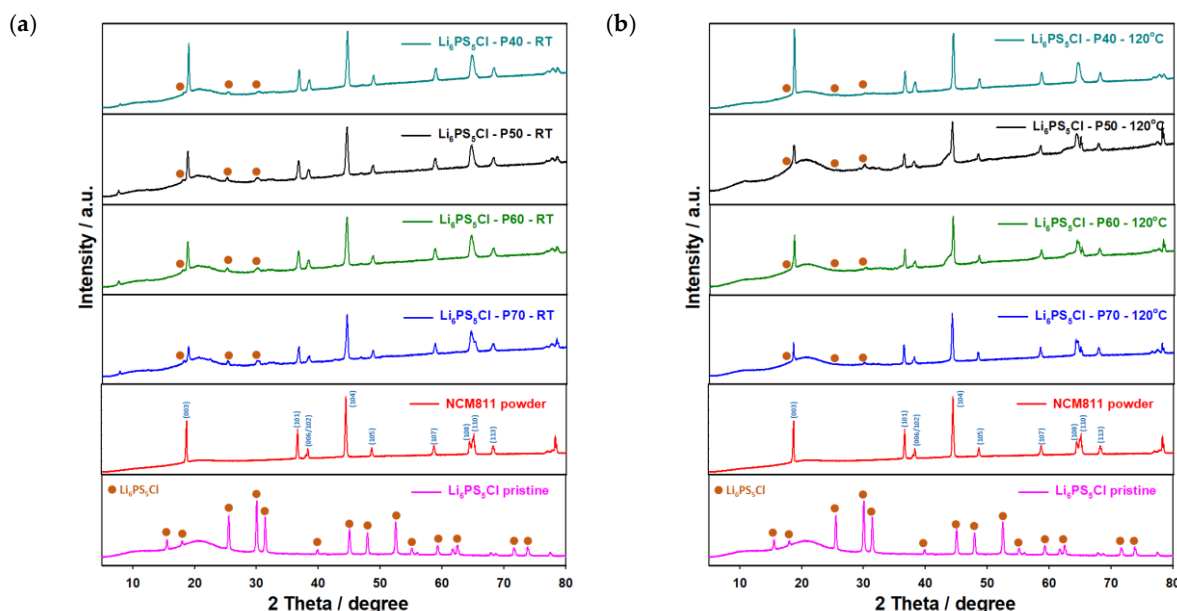


**Figure 5.** XRD patterns of NMC811 electrodes infiltrated with Li<sub>6</sub>PS<sub>5</sub>Cl after drying at (a) room temperature and (b) 120 °C for 2 h in a vacuum.

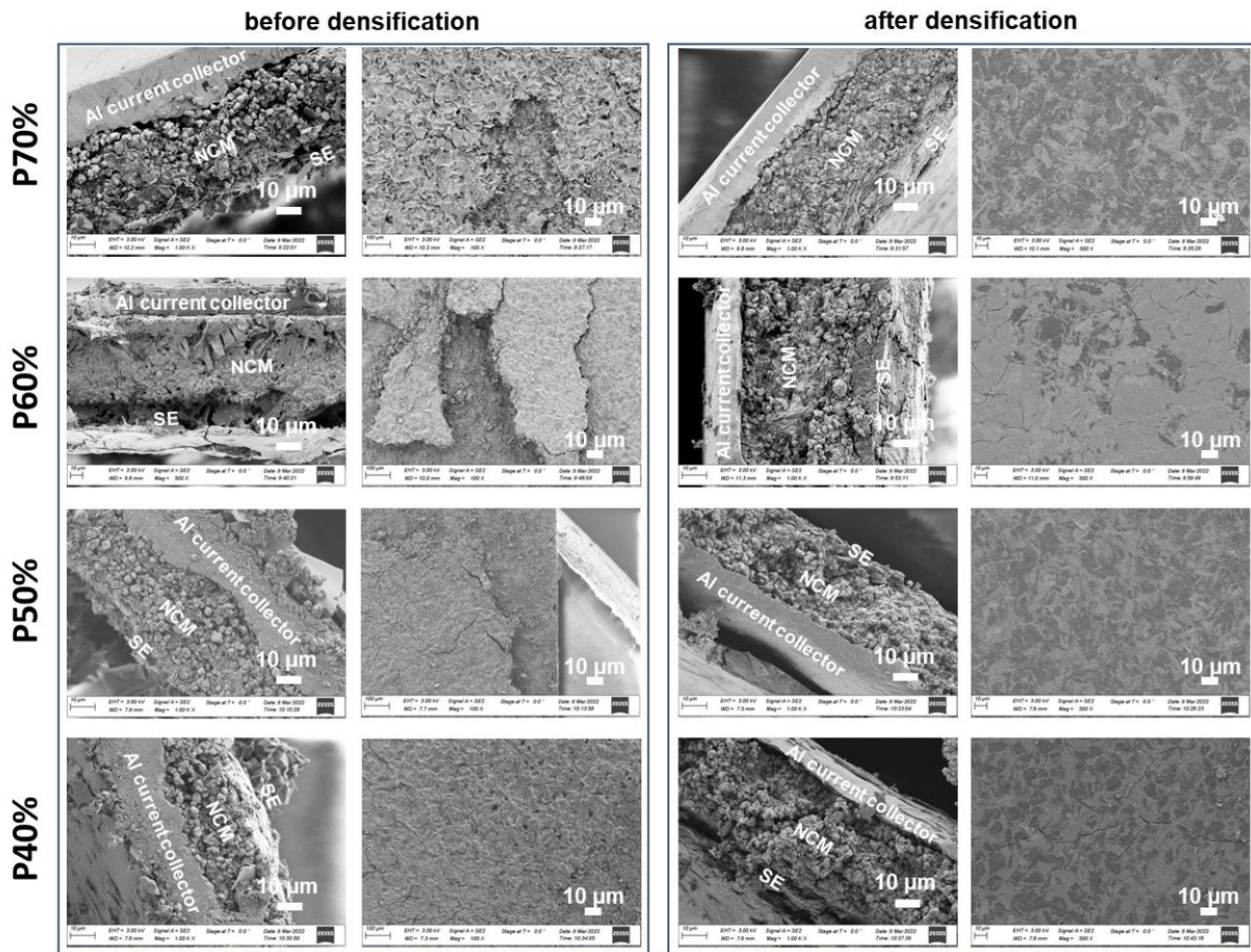


**Figure 6.** SEM images and cross-section of the NCM electrode materials with immersed solid electrolyte (NCM/solid electrolyte later) and their compatibility via ethanol solution before and applied pressing.

As shown by the cross-sectional EDX images in Figure 7, it is evident that most of the electrolyte crystallized on the electrode surfaces rather than within the pores. Notably, the NCM electrodes infiltrated by solid electrolytes before densification showed a uniform distribution of the elements of  $\text{Li}_6\text{PS}_5\text{Cl}$  electrolyte. After densification, the NCM electrodes show the main concentration of the solid electrolyte on the electrode surfaces due to the large particles and plate-like-shaped particles of  $\text{Li}_6\text{PS}_5\text{Cl}$  after ethanol treatment (Figure 7a). The elemental mapping makes it clearly visible that the  $\text{Li}_6\text{PS}_5\text{Cl}$  mainly segregates at the surface of the electrodes rather than penetrating into the bulk and filling the pores. Especially for the densified sample, all the elements associated with the  $\text{Li}_6\text{PS}_5\text{Cl}$  material can be found on the surface of the electrode (Figure 7b). A low porosity (40 wt%) compared to the 70 wt% electrode further limits the infiltration of the SE solution into the electrode (Figure 7c).

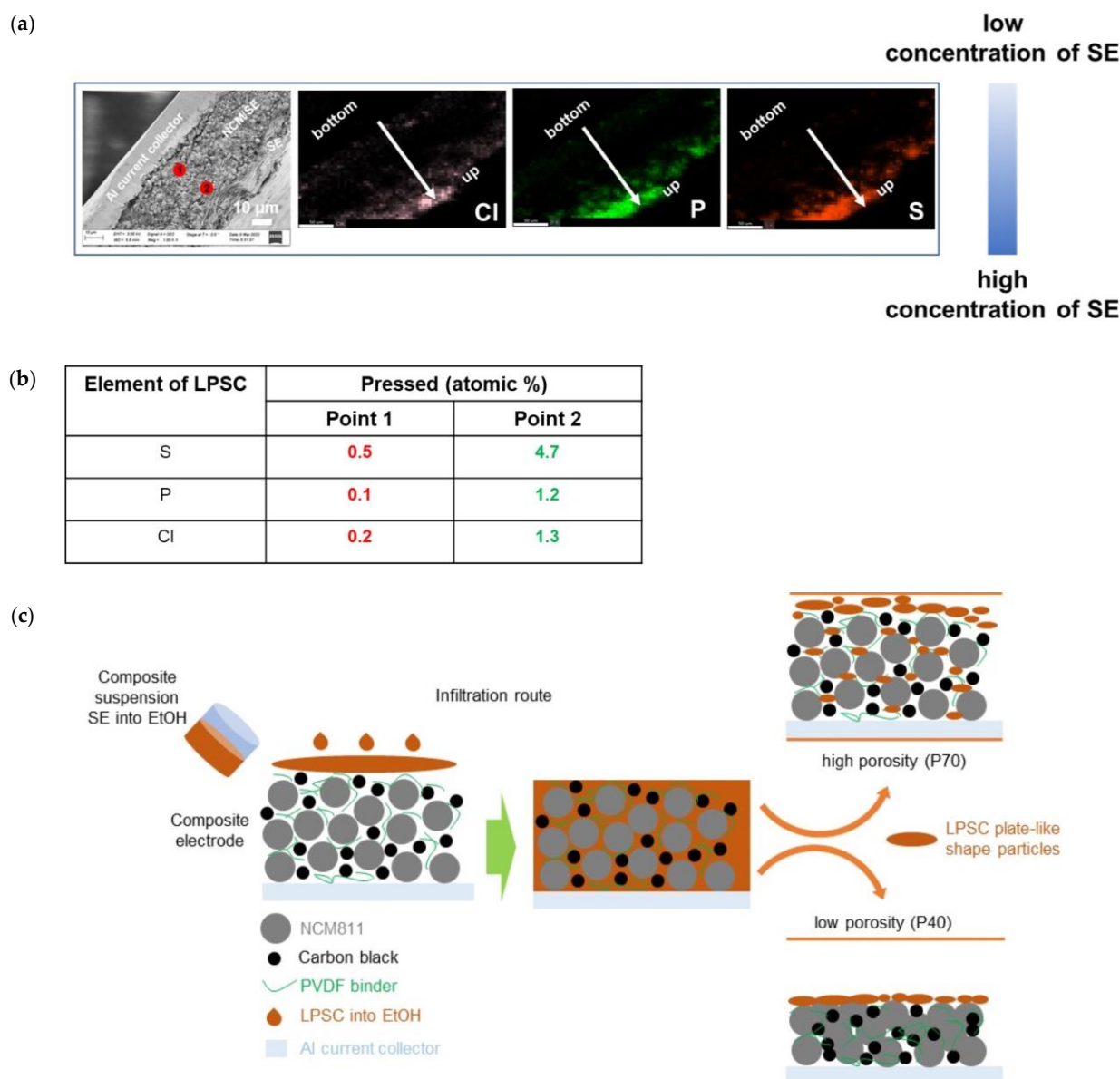


**Figure 7.** (a) EDX results for the infiltrated NCM811 electrode showing 70% porosity after densification. (b) The elemental distribution for 2 points located close to the electrode surface and close to the current collector is given. (c) Schematic illustration of the infiltration process of  $\text{Li}_6\text{PS}_5\text{Cl}$  solution into the conventional lithium-ion battery electrodes.

To confirm the contact between the cathode material and infiltrated solid electrolytes and elucidate the lithium-ion transport kinetics, EIS measurements were performed. As shown in Figure 8a, the Nyquist plots of the NCM samples with different porosity values were obtained in a fresh state and fitted by the equivalent circuit with more discussion about the influence of each element on the surface resistivity [15,55]. Regarding the equivalent circuit for obtained samples, resistances are identified with the R<sub>1</sub> as the solid electrolyte layer between the cathode (R<sub>c</sub> as R<sub>2</sub> is path resistance and R<sub>3</sub> as the interfacial resistance) and anode (R<sub>a</sub> as R<sub>4</sub> is an interface between the lithium anode and solid electrolyte), and Warburg (W) impedance as shown in Figure 8b and by the obtained values in Table 3. It should be noted that for the sample with the low-porosity (P40) active material, the resistances of R<sub>2</sub> and R<sub>3</sub> have a limiting impact on the charge transfer between the cathode and solid electrolyte due to lower penetration of the solid electrolyte during the infiltration process; this solid electrolyte layer works as an insulating layer, which prevents and restricts

lithium-ion transportation capability compared to the sample with high porosity (P70) as presented in Table 3. The resistance of the solid electrolyte (R1) is decreasing from low to high porosity values of the NCM cathode due to the penetration of the solid electrolyte into the cathode composite (Figure 8a). Moreover, the increase in the path resistance (R2) from P70 to P40 is related to the porosity and pathways of solid electrolytes during the infiltration process into the deepening of the cathode composite. The resistance of R4 (Ra) is reflected in the resistance of the lithium anode and solid electrolyte, increasing from low cathode porosity to high due to the microstructure of the cathode composite and reduced contact between the lithium anode and solid electrolyte [56]. It should be noted that the solid electrolyte with high ionic conductivity allows the charging and discharging of the thick lithium-ion battery cathode (800  $\mu\text{m}$ ) in a solid-state battery configuration as shown in [56]. However, the infiltration route of solid electrolytes into conventional lithium-ion battery cathode electrodes may depend on the solvent evaporation effect, mixed solvents, the surface morphology of solid electrolytes, particle size, and porosity of cathode composite.

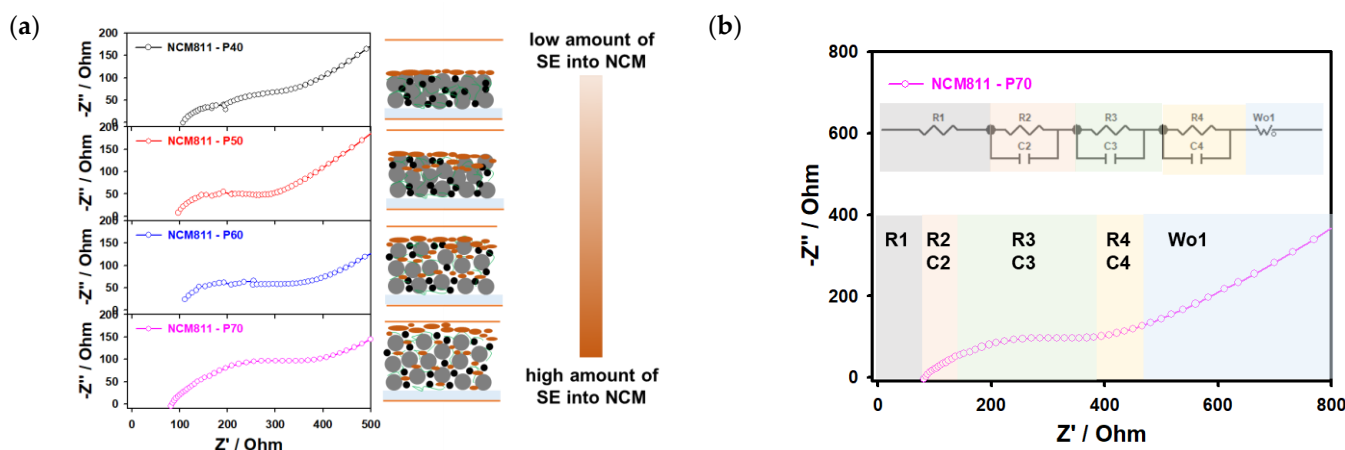


**Figure 8.** (a) Electrochemical impedance spectrum with the equivalent circuit model and (b) Nyquist plots of the NMC811 electrodes infiltrated with  $\text{Li}_6\text{PS}_5\text{Cl}$  solid electrolyte.

**Table 3.** Resistance values and specific capacities of infiltrated composite cathode with porosity values of 70%, 60%, 50%, and 40%.

Porosity of Electrode after Calendaring, %	EIS Resistance, Ohm					Adhesion between NCM811/SE and SE Film	
	R1 (SE Electrolyte)	Rc (Interface between CAM and SE)		(R4) Ra (Interface between AM and SE)	Specific Capacity, $\text{mAh g}^{-1}$		
		R2 (Path Resistance)	R3 (Interfacial Resistance)				
P70	88.3	59.1	155.7	109.4	3.10	poor	
P60	112.4	61.8	78.9	93.9	2.64	poor	
P50	102.9	68.1	73.9	83.9	2.06	medium	
P40	117.6	73.4	62.7	65.1	0.06	good	

It was noticed that the sample with a high porosity value of P70 has better contact within the infiltrated solid electrolyte cathode composite than the other samples. However, all samples show slightly lower specific capacities due to the formation of large particles and plate-like-shaped particles of  $\text{Li}_6\text{PS}_5\text{Cl}$  after ethanol treatment shown in Figures 4 and 6. Lithium-ion diffusion through the solid electrolyte layer formed on the surface of the cathode and infiltrating the solid electrolyte can significantly improve cyclic stability; however, due to the formation of the large particles, it leads to capacity fading after the first cycle in order to allow this solid electrolyte layer to function as an insulating layer, which prevents lithium-ion transport (Figure 9). It should be noted that the infiltration

of the LPSC electrolyte into conventional lithium-ion battery NCM electrodes leads to poor electrochemical performance due to the formation of plate-like LPSC particles, the complicated infiltration process, and the fact that infiltrated LPSC electrolytes are working as an insulating layer (Figure 9). At the same time, non-infiltrated conventional LIB NCM electrodes exhibit extremely low performance due to sluggish lithium kinetics when compared to cells with all-solid-state battery components [26]. Based on the obtained results, we proposed a mechanism for the infiltration process of the solid electrolyte into the cathode composite with various values of porosity, as shown in Figures 7 and 9. Therefore, we can assume that the infiltration route of the solid electrolyte into conventional cathode electrodes of lithium-ion batteries may depend on the solvent evaporation effect, the solvent mixture, the surface morphology of the solid electrolyte, and the particle size of the cathodes. This behavior will be of great importance in the fabrication of commercial electrodes based on conventional binders and solvent systems for achieving high capacity, long cycle life, safety, and scalable solid-state batteries with sulfide-based solid electrolytes.

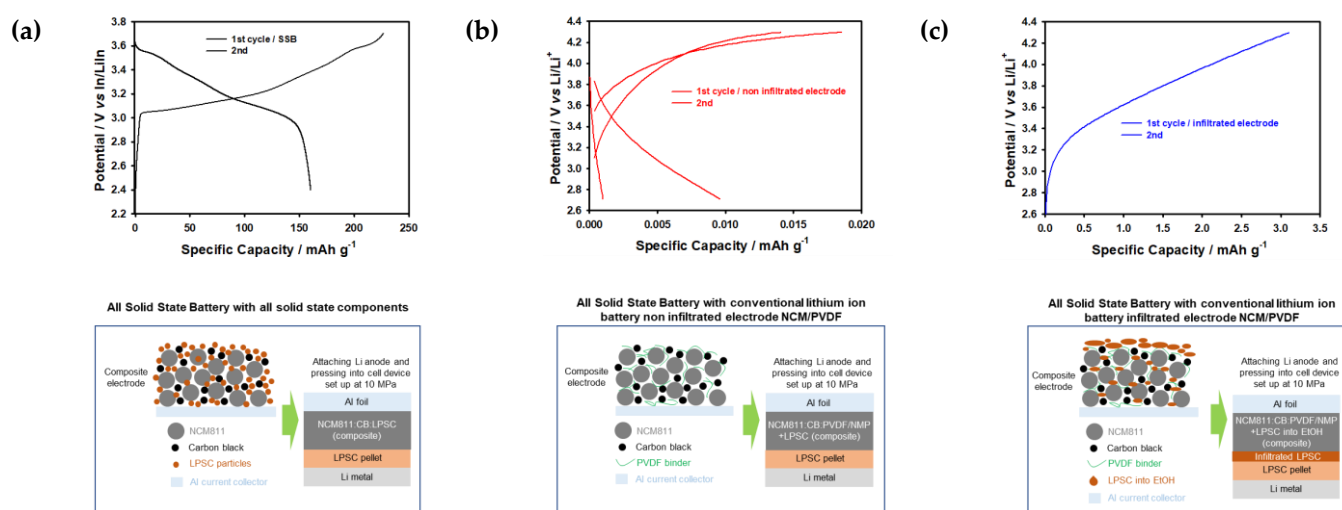


**Figure 9.** First charge and discharge curves for (a) all-solid-state battery, (b) non-infiltrated, and (c) infiltrated cathodes.

#### 4. Conclusions

In summary, we can conclude that the infiltration process does not yield superior composite electrodes compared to conventional electrode preparation. The dissolution and reprecipitation of  $\text{Li}_6\text{PS}_5\text{Cl}$  using ethanol as a solvent yield ionic conductivity reductions in the order of one magnitude. Furthermore, processability issues were encountered, and the penetration of the electrolyte solution into the pores of conventional electrodes could not be observed. We suggest, based on the obtained results, that the development of various solution-processable SEs has high ionic conductivity or close to pristine solid electrolytes and good compatibility with electrode components, which are still needed for the improvement of this process. Therefore, it is expected that the infiltration route of the solid electrolyte into conventional electrodes can depend on the solvent vaporization effect, mixed solvents, the surface morphology of the solid electrolyte, and particle sizes of cathodes, which will be of great significance in the fabrication of commercial electrodes for achieving high capacity, long cycle life, safety, and scalable solid-state batteries with sulfide-based solid electrolytes.

**Supplementary Materials:** The following supporting information can be downloaded at: <https://www.mdpi.com/article/10.3390/batteries9100503/s1>, Figure S1—XRD pattern, SEM, XRF, Rate capabilities, and voltage curves of the NCM811-coated  $\text{LiNbO}_3$  electrode. Figure S2—Solution of solid electrolyte of  $\text{Li}_6\text{PS}_5\text{Cl}$  into ethanol. Table S1—Solvent and solvent systems. Figure S3—Nyquist plots of the pristine used for EIS measurements of  $\text{Li}_6\text{PS}_5\text{Cl}$  samples. Figure S4—SEM images of solid

electrolyte. Figure S5—XRD patterns of solid electrolyte. Figure S6—The NCM811 electrode materials with immersed solid electrolyte. Figure S7—The NCM811 electrode materials with immersed solid electrolyte [57–59].

**Author Contributions:** Conceptualization: A.T. and A.B.; methodology: A.T. and A.B.; general experimental investigation and electrochemical analysis: A.T. and A.B.; characterization XRD: A.T. and A.B.; characterization SEM: A.T. and A.B.; writing—original draft preparation: A.T. and A.B.; writing—review and editing: A.T., A.B. and A.P. All authors have read and agreed to the published version of the manuscript.

**Funding:** The SUBLIME project is funded by the European Union’s H2020 research and innovation programme under Grant Agreement no. 875028. Furthermore, the authors want to express their gratitude to Ningxin Zhang for the SEM/EDX analysis of samples and Raad Hamid for the XRD measurements of obtained samples.

**Data Availability Statement:** Not applicable.

**Acknowledgments:** The authors want to express their gratitude to Jacqueline Winter for linguistic proofreading and corrections.

**Conflicts of Interest:** The authors declare no conflict of interest.

## References

1. Horowitz, Y.; Schmidt, C.; Yoon, D.-H.; Riegger, L.M.; Katzenmeier, L.; Bosch, G.M.; Noked, M.; Ein-Eli, Y.; Janek, J.; Zeier, W.G.; et al. Between liquid and all solid: A prospect on electrolyte future in lithium-ion batteries for electric vehicles. *Energy Technol.* **2020**, *8*, 2000580. [[CrossRef](#)]
2. Goodenough, J.B.; Kim, Y. Challenges for rechargeable Li batteries. *Chem. Mater.* **2009**, *22*, 587–603. [[CrossRef](#)]
3. Xia, G.B.; Cao, L.; Bi, G.L. A review on battery thermal management in electric vehicle application. *J. Power Sources* **2017**, *367*, 90–105. [[CrossRef](#)]
4. Banerjee, A.; Wang, X.; Fang, C.; Wu, E.A.; Meng, Y.S. Interfaces and interphases in all-solid-state batteries with inorganic solid electrolytes. *Chem. Rev.* **2020**, *120*, 6878–6933. [[CrossRef](#)]
5. Lu, Y.; Zhao, C.Z.; Yuan, H.; Cheng, X.B.; Huang, J.Q.; Zhang, Q. Critical current density in solid-state lithium metal batteries: Mechanism, influences, and strategies. *Adv. Funct. Mater.* **2021**, *31*, 2009925. [[CrossRef](#)]
6. Tron, A.; Nosenko, A.; Park, Y.D.; Mun, J. Synthesis of the solid electrolyte  $\text{Li}_2\text{O}-\text{LiF}-\text{P}_2\text{O}_5$  and its application for lithium-ion batteries. *Solid State Ion.* **2017**, *308*, 40–45. [[CrossRef](#)]
7. Tron, A.; Nosenko, A.; Park, Y.D.; Mun, J. The solid electrolytes  $\text{Li}_2\text{O}-\text{LiF}-\text{Li}_2\text{WO}_4-\text{B}_2\text{O}_3$  with enhanced ionic conductivity for lithium-ion battery. *J. Ind. Eng. Chem.* **2019**, *73*, 62–66. [[CrossRef](#)]
8. López-Aranguren, P.; Reynaud, M.; Ghuchowski, P.; Bustinza, A.; Galceran, M.; López del Amo, J.M.; Armand, M.; Casas-Cabanas, M. Crystalline LiPON as a bulk-type solid electrolyte. *ACS Energy Lett.* **2021**, *6*, 445–450. [[CrossRef](#)]
9. Deng, Y.; Eames, C.; Fleutot, B.; David, R.; Chotard, J.-N.; Suard, E.; Masquelier, C.; Saiful Islam, M. Enhancing the lithium ion conductivity in lithium superionic Conductor (LISICON) solid electrolytes through a mixed polyanion effect. *ACS Appl. Mater. Interfaces* **2017**, *8*, 7050–7058. [[CrossRef](#)]
10. Tao, B.; Ren, C.; Li, H.; Liu, B.; Jia, X.; Dong, X.; Zhang, S.; Chang, H. Thio-/LISICON and LGPS-type solid electrolytes for all-solid-state lithium-ion batteries. *Adv. Funct. Mater.* **2022**, *32*, 2203551. [[CrossRef](#)]
11. Oh, J.A.S.; He, L.; Plewa, A.; Morita, M.; Zhao, Y.; Sakamoto, T.; Song, X.; Zhai, W.; Zeng, K.; Lu, L. Composite NASICON ( $\text{Na}_3\text{Zr}_2\text{Si}_2\text{PO}_{12}$ ) solid-state electrolyte with enhanced  $\text{Na}^+$  ionic conductivity: Effect of liquid phase sintering. *ACS Appl. Mater. Interfaces* **2019**, *43*, 40125–40133. [[CrossRef](#)] [[PubMed](#)]
12. Wang, C.; Fu, K.; Kammampata, S.P.; McOwen, D.W.; Samson, A.J.; Zhang, L.; Hitz, G.T.; Nolan, A.M.; Wachsman, E.D.; Mo, Y.; et al. Garnet-type solid-state electrolytes: Materials, interfaces, and batteries. *Chem. Rev.* **2020**, *120*, 4257–4300. [[CrossRef](#)] [[PubMed](#)]
13. Lu, J.; Li, Y. Perovskite-type Li-ion solid electrolytes: A review. *J. Mater. Sci. Mater. Electron.* **2021**, *32*, 9736–9754. [[CrossRef](#)]
14. Kwak, H.; Wang, S.; Park, J.; Liu, Y.; Kim, K.T.; Choi, Y.; Mo, Y.; Jung, Y.S. Emerging halide superionic conductors for all-solid-state batteries: Design, synthesis, and practical applications. *ACS Energy Lett.* **2022**, *7*, 1776–1805. [[CrossRef](#)]
15. Kim, K.J.; Balaish, M.; Wadaguchi, M.; Kong, L.; Rupp, J.L.M. Solid-state Li–metal batteries: Challenges and horizons of oxide and sulfide solid electrolytes and their interfaces. *Adv. Energy Mater.* **2021**, *11*, 2002689. [[CrossRef](#)]
16. Adeli, P.; Bazak, J.D.; Park, K.H.; Kochetkov, I.; Huq, A.; Goward, G.R.; Nazar, L.F. Boosting solid-state diffusivity and conductivity in lithium superionic argyrodites by halide substitution. *Angew. Chem. Int. Ed.* **2019**, *58*, 8681–8686. [[CrossRef](#)]
17. Xu, R.C.; Wang, X.L.; Zhang, S.Z.; Xia, Y.; Xia, X.H.; Wu, J.B.; Tu, J.P. Rational coating of  $\text{Li}_7\text{P}_3\text{S}_{11}$  solid electrolyte on  $\text{MoS}_2$  electrode for all-solid-state lithium ion batteries. *J. Power Source* **2018**, *374*, 107–112. [[CrossRef](#)]
18. Tao, B.; Zhong, D.; Li, H.; Wang, G.; Chang, H. Halide solid-state electrolytes for all-solid-state batteries: Structural design, synthesis, environmental stability, interface optimization and challenges. *Chem. Sci.* **2023**, *14*, 8693–8722. [[CrossRef](#)]

19. Lee, K.; Kim, S.; Park, J.; Park, S.H.; Coskun, A.; Jung, D.S.; Cho, W.; Choi, J.W. Selection of binder and solvent for solution-processed all-solid-state battery. *J. Electrochem. Soc.* **2017**, *164*, A2075. [[CrossRef](#)]
20. Koç, T.; Marchini, F.; Rousse, G.; Dugas, R.; Tarascon, J.-M. In the search for the best solid electrolyte-layered oxide pairing for assembling practical all-solid-state batteries. *ACS Appl. Energy Mater.* **2021**, *12*, 13575–13585. [[CrossRef](#)]
21. Nam, Y.J.; Oh, D.Y.; Jung, S.H.; Jung, Y.S. Toward practical all-solid-state lithium-ion batteries with high energy density and safety: Comparative study for electrodes fabricated by dry- and slurry-mixing processes. *J. Power Sources* **2018**, *375*, 93–101. [[CrossRef](#)]
22. Lu, Y.; Zhao, C.-Z.; Yuan, H.; Hu, J.-K.; Huang, J.-Q.; Zhang, Q. Dry electrode technology, the rising star in solid-state battery industrialization. *Matter* **2022**, *5*, 876–898. [[CrossRef](#)]
23. Kim, K.T.; Kwon, T.Y.; Jung, Y.S. Scalable fabrication of sheet-type electrodes for practical all-solid-state batteries employing sulfide solid electrolytes. *Curr. Opin. Electrochem.* **2022**, *34*, 101026. [[CrossRef](#)]
24. Cai, Y.; Li, C.; Zhao, Z.; Mu, D.; Wu, B. Air stability and interfacial compatibility of sulfide solid electrolytes for solid-state lithium batteries: Advances and perspectives. *ChemElectroChem* **2022**, *9*, e202101479. [[CrossRef](#)]
25. Chen, Y.-T.; Marple, M.A.T.; Tan, D.H.S.; Ham, S.-Y.; Sayahpour, B.; Li, W.-K.; Yang, H.; Lee, J.B.; Hah, H.J.; Wu, E.A.; et al. Investigating dry room compatibility of sulfide solid-state electrolytes for scalable manufacturing. *J. Mater. Chem. A* **2022**, *10*, 7155–7164. [[CrossRef](#)]
26. Tron, A.; Hamid, R.; Zhang, N.; Beutl, A. Rational optimization of cathode composites for sulfide-based all-solid-state batteries. *Nanomaterials* **2023**, *13*, 327. [[CrossRef](#)]
27. Han, Y.; Jung, S.H.; Kwak, H.; Jun, S.; Kwak, H.H.; Lee, J.H.; Hong, S.-T.; Jung, Y.S. Single- or poly-crystalline Ni-rich layered cathode, sulfide or halide solid electrolyte: Which will be the winners for all-solid-state batteries? *Adv. Energy Mater.* **2021**, *11*, 2100126. [[CrossRef](#)]
28. Tan, D.H.S.; Banerjee, A.; Deng, Z.; Wu, E.A.; Nguyen, H.; Doux, J.-M.; Wang, X.; Cheng, J.-H.; Ong, S.P.; Meng, Y.S.; et al. Enabling thin and flexible solid-state composite electrolytes by the scalable solution process. *ACS Appl. Energy Mater.* **2019**, *2*, 6542–6550. [[CrossRef](#)]
29. Oh, D.Y.; Nam, Y.J.; Park, K.H.; Jung, S.H.; Kim, K.T.; Ha, A.R.; Jung, Y.S. Slurry-fabricable  $\text{Li}^+$ -conductive polymeric binders for practical all-solid-state lithium-ion batteries enabled by solvate ionic liquids. *Adv. Energy Mater.* **2019**, *9*, 1802927. [[CrossRef](#)]
30. Tron, A.; Hamid, R.; Zhang, N.; Paoella, A.; Wulfert-Holzmann, P.; Kolotygin, V.; López-Aranguren, P.; Beutl, A. Film processing of  $\text{Li}_6\text{PS}_5\text{Cl}$  electrolyte using different binders and their combinations. *J. Energy Storage* **2023**, *66*, 107480. [[CrossRef](#)]
31. Nikodimos, Y.; Huang, C.-J.; Taklu, B.W.; Su, W.-N.; Hwang, B.J. Chemical stability of sulfide solid-state electrolytes: Stability toward humid air and compatibility with solvents and binders. *Energy Environ. Sci.* **2022**, *15*, 991–1033. [[CrossRef](#)]
32. Inada, T.; Takada, K.; Kajiyama, A.; Kouguchi, M.; Sasaki, H.; Kondo, S.; Watanabe, M.; Murayama, M.; Kanno, R. Fabrications and properties of composite solid-state electrolytes. *Solid State Ion.* **2003**, *158*, 275–280. [[CrossRef](#)]
33. Kim, D.H.; Oh, D.Y.; Park, K.H.; Choi, Y.E.; Nam, Y.J.; Lee, H.A.; Lee, S.-M.; Jung, Y.S. Infiltration of solution-processable solid electrolytes into conventional Li-ion-battery electrodes for all-solid-state Li-ion batteries. *Nano Lett.* **2017**, *17*, 3013–3020. [[CrossRef](#)] [[PubMed](#)]
34. Kim, D.H.; Lee, H.A.; Song, Y.B.; Park, J.W.; Lee, S.-M.; Jung, Y.S. Sheet-type  $\text{Li}_6\text{PS}_5\text{Cl}$ -infiltrated Si anodes fabricated by solution process for all-solid-state lithium-ion batteries. *J. Power Sources* **2019**, *426*, 143–150. [[CrossRef](#)]
35. Kim, M.-J.; Park, J.-W.; Kim, B.G.; Lee, Y.-J.; Ha, Y.-C.; Lee, S.-M.; Baeg, K.-J. Facile fabrication of solution-processed solid-electrolytes for high-energy-density all-solid-state-batteries by enhanced interfacial contact. *Sci. Rep.* **2020**, *10*, 11923. [[CrossRef](#)]
36. Li, X.; Jin, L.; Song, D.; Zhang, H.; Shi, X.; Wang, Z.; Zhang, L.; Zhu, L.  $\text{LiNbO}_3$ -coated  $\text{LiNi}_{0.8}\text{Co}_{0.1}\text{Mn}_{0.1}\text{O}_2$  cathode with high discharge capacity and rate performance for all-solid-state lithium battery. *J. Energy Chem.* **2020**, *40*, 39–45. [[CrossRef](#)]
37. Ohta, N.; Takada, K.; Sakaguchi, I.; Zhang, L.; Ma, R.; Fukuda, K.; Osada, M.; Sasaki, T.  $\text{LiNbO}_3$ -coated  $\text{LiCoO}_2$  as cathode material for all solid-state lithium secondary batteries. *Electrochim. Commun.* **2007**, *9*, 1486–1490. [[CrossRef](#)]
38. Li, Y.; Li, X.; Hu, J.; Liu, W.; Sari, H.M.K.; Li, D.; Sun, Q.; Kou, L.; Tian, Z.; Shao, L.; et al.  $\text{ZnO}$  interface modified  $\text{LiNi}_{0.6}\text{Co}_{0.2}\text{Mn}_{0.2}\text{O}_2$  toward boosting lithium storage. *Energy Environ. Mater.* **2020**, *3*, 522–528. [[CrossRef](#)]
39. Tron, A.; Hong, M.; Park, Y.D.; Kim, J.; Mun, J. Ni-rich layered cathode materials by a mechanochemical method for high-energy Lithium-ion batteries. *ChemistrySelect* **2020**, *5*, 14596–14601. [[CrossRef](#)]
40. Tron, A.; Park, Y.D.; Mun, J.  $\text{AlF}_3$ -coated  $\text{LiMn}_2\text{O}_4$  as cathode material for aqueous rechargeable lithium battery with improved cycling stability. *J. Power Sources* **2016**, *325*, 360–364. [[CrossRef](#)]
41. Jaiser, S.; Müller, M.; Baunach, M.; Bauer, W.; Scharfer, P.; Schabel, W. Investigation of film solidification and binder migration during drying of Li-Ion battery anodes. *J. Power Sources* **2016**, *318*, 210–219. [[CrossRef](#)]
42. Tan, D.H.S.; Wu, E.A.; Nguyen, H.; Chen, Z.; Marple, M.A.T.; Doux, J.M.; Wang, X.; Yang, H.; Banerjee, A.; Meng, Y.S. Elucidating reversible electrochemical redox of  $\text{Li}_6\text{PS}_5\text{Cl}$  solid electrolyte. *ACS Energy Lett.* **2019**, *4*, 2418–2427. [[CrossRef](#)]
43. Ruhl, J.; Rieger, L.M.; Ghidiu, M.; Zeier, W.G. Impact of solvent treatment of the superionic argyrodite  $\text{Li}_6\text{PS}_5\text{Cl}$  on solid-state battery performance. *Adv. Energy Sustain. Res.* **2021**, *2*, 2000077. [[CrossRef](#)]
44. Koerver, R.; Aygün, I.; Leichtweiß, T.; Dietrich, C.; Zhang, W.; Binder, J.O.; Hartmann, P.; Zeier, W.G.; Janek, J. Capacity fade in solid-state batteries: Interphase formation and chemomechanical processes in nickel-rich layered oxide cathodes and lithium thiophosphate solid electrolytes. *Chem. Mater.* **2017**, *29*, 5574–5582. [[CrossRef](#)]
45. Zhang, Z.; Zhang, L.; Liu, Y.; Yan, X.; Xu, B.; Wang, L.-M. One-step solution process toward formation of  $\text{Li}_6\text{PS}_5\text{Cl}$  argyrodite solid electrolyte for all-solid-state lithium-ion batteries. *J. Alloys Comp.* **2020**, *812*, 152103. [[CrossRef](#)]

46. Giraldo, S.; Nakagawa, K.; Vásquez, F.A.; Fujii, Y.; Wang, Y.; Miura, A.; Calderón, J.A.; Rosero-Navarro, N.C.; Tadanaga, K. Preparation of composite electrodes for all-solid-state batteries based on sulfide electrolytes: An electrochemical point of view. *Batteries* **2021**, *7*, 77. [[CrossRef](#)]
47. Rosero-Navarro, N.C.; Miura, A.; Tadanaga, K. Preparation of lithium ion conductive  $\text{Li}_6\text{PS}_5\text{Cl}$  solid electrolyte from solution for the fabrication of composite cathode of all-solid-state lithium battery. *J. Sol-Gel Sci. Technol.* **2019**, *89*, 303–309. [[CrossRef](#)]
48. Rosero-Navarro, N.C.; Miura, A.; Tadanaga, K. Composite cathode prepared by argyrodite precursor solution assisted by dispersant agents for bulk-type all-solid-state batteries. *J. Power Sources* **2018**, *396*, 33–40. [[CrossRef](#)]
49. Yubuchi, S.; Teragawa, S.; Aso, K.; Tadanaga, K.; Hayashi, A.; Tatsumisago, M. Preparation of high lithium-ion conducting  $\text{Li}_6\text{PS}_5\text{Cl}$  solid electrolyte from ethanol solution for all-solid-state lithium batteries. *J. Power Sources* **2015**, *293*, 941–945. [[CrossRef](#)]
50. Zhou, L.; Park, K.-H.; Sun, X.; Lalère, F.; Adermann, T.; Hartmann, P.; Nazar, L. Solvent-engineered design of argyrodite  $\text{Li}_6\text{PS}_5\text{X}$  ( $\text{X} = \text{Cl}, \text{Br}, \text{I}$ ) solid electrolytes with high ionic conductivity. *ACS Energy Lett.* **2019**, *4*, 265–270. [[CrossRef](#)]
51. Carbone, L.; Verrelli, R.; Gobet, M.; Peng, J.; Devany, M.; Scrosati, B.; Greenbaum, S.; Hassoun, J. Insight on the  $\text{Li}_2\text{S}$  electrochemical process in a composite configuration electrode. *New J. Chem.* **2016**, *40*, 2935–2943. [[CrossRef](#)] [[PubMed](#)]
52. Tron, A.; Jo, Y.N.; Oh, S.H.; Park, Y.D.; Mun, J. Surface modification of the  $\text{LiFePO}_4$  cathode for the aqueous rechargeable lithium ion battery. *ACS Appl. Mater. Interfaces* **2017**, *9*, 12391–12399. [[CrossRef](#)] [[PubMed](#)]
53. Belharouak, I.; Johnson, C.; Amine, K. Synthesis and electrochemical analysis of vapor-deposited carbon-coated  $\text{LiFePO}_4$ . *Electrochim. Commun.* **2005**, *7*, 983–988. [[CrossRef](#)]
54. Wang, S.; Zhang, Y.; Zhang, X.; Liu, T.; Lin, Y.-H.; Shen, Y.; Li, L.; Nan, C.-W. High-conductivity argyrodite  $\text{Li}_6\text{PS}_5\text{Cl}$  solid electrolytes prepared via optimized sintering processes for all-solid-state lithium–sulfur batteries. *ACS Appl. Mater. Interfaces* **2018**, *10*, 42279–42285. [[CrossRef](#)]
55. Asano, T.; Sakai, A.; Ouchi, S.; Sakaida, M.; Miyazaki, A.; Hasegawa, S. Solid halide electrolytes with high lithium-ion conductivity for application in 4 V class bulk-type all-solid-state batteries. *Adv. Mater.* **2018**, *30*, 1803075. [[CrossRef](#)]
56. Li, Y.; Song, S.; Kim, H.; Nomoto, K.; Kim, H.; Sun, X.; Hori, S.; Suzuki, K.; Matsui, N.; Hirayama, M.; et al. A lithium superionic conductor for millimeter-thick battery electrode. *Science* **2023**, *381*, 50–53. [[CrossRef](#)]
57. Dielectric Constant of Common solvents.xls. Available online: [washington.edu](http://washington.edu) (accessed on 20 September 2023).
58. Dielectric Constant Table.pdf. Available online: [honeywellprocess.com](http://honeywellprocess.com) (accessed on 20 September 2023).
59. Physicochemical Properties of Solvents. Available online: [SigmaAldrich.com](http://SigmaAldrich.com) (accessed on 20 September 2023).

**Disclaimer/Publisher’s Note:** The statements, opinions and data contained in all publications are solely those of the individual author(s) and contributor(s) and not of MDPI and/or the editor(s). MDPI and/or the editor(s) disclaim responsibility for any injury to people or property resulting from any ideas, methods, instructions or products referred to in the content.